Available online at www.sciencedirect.com
ScienceDirect
Journal of Computational Physics 221 (2007) 506–523
JOURNAL OF COMPUTATIONAL PHYSICS
www.elsevier.com/locate/jcp

A numerical method for capillarity-dominant free surface flows

Albert Y. Tong *, Zhaoyuan Wang

Department of Mechanical and Aerospace Engineering, University of Texas, Arlington, TX 76019, USA

Received 2 February 2006; received in revised form 6 June 2006; accepted 18 June 2006
Available online 8 August 2006

Abstract

The continuum surface force (CSF) method has been extensively employed in the volume-of-fluid (VOF), level set (LS) and front tracking methods to model the surface tension force. It is a robust method requiring relatively easy implementation. However, it is known to generate spurious currents near the interface, which may lead to disastrous interface instabilities and failures of grid convergence. A different surface tension implementation algorithm, referred to as the pressure boundary method (PBM), is introduced in this study. The surface tension force is incorporated into the Navier–Stokes equation via a pressure gradient while the free surface is tracked by a coupled level set and volume-of-fluid (CLSVOF) method. It has been shown that the spurious currents are greatly reduced by the PBM method with the sharp pressure boundary condition preserved. The numerical results of several test cases have been obtained and are in close agreement with data reported in the literature.

Keywords: Volume-of-fluid; Level set; Surface tension; Free surface flows

1. Introduction

Free surface flows appear in various industrial applications such as inkjet printing, atomization, blending, flow coating, internal engine fuel spraying and container filling. The main difficulty arising in the numerical simulation of this type of flow is the determination of the precise location of the free surface where boundary conditions are applied. In recent years, a number of methods have been developed for modeling such free surface flows [1], which can be classified primarily as Lagrangian or Eulerian-based. In general, Lagrangian-based methods track the free surface and offer the precise location of the free surface. They are not suited for flows that involve merging and separation of free surface. On the other hand, Eulerian-based methods capture, rather than track, the free surface. They are better suited for flows with complex topological changes and interface deformations. The volume-of-fluid (VOF) method [2] and the level set (LS) method [3] are two Eulerian-based methods that have been widely used. Both methods utilize a phase function to track the interface implicitly, namely, volume fraction for the VOF method and distance function for the LS method.

* Corresponding author. Tel.: +1 817 272 2297; fax: +1 817 272 2952.
E-mail address: tong@uta.edu (A.Y. Tong).

0021-9991/$ - see front matter
doi:10.1016/j.jcp.2006.06.034

Surface tension effect plays a significant role in some important free surface flow problems such as droplet deformation, bubble motion and liquid ligament breakup. The continuum surface force (CSF) model [4] has been widely used to model surface tension. In the CSF model, surface tension effect is treated as a body force, $\vec{F}_b$. It is distributed within a transition region of finite thickness at the interface, given by:

$$\vec{F}_b = \sigma\kappa\vec{n}\delta(\vec{x}) \tag{1}$$

where σ is the coefficient of surface tension, κ the mean curvature, $\vec{n}$ the normal to the surface, and $\delta(\vec{x})$ a delta function concentrated at the interface. In the context of the VOF method, the body force is given by:

$$\vec{F}_b = \sigma\kappa\nabla F \tag{2}$$

where F is the VOF function. It is included in the momentum equation as a source term. This continuum treatment of the discontinuous change at the interface eases the implementation of the surface tension effect where only the VOF function or the LS function is needed. In problems with complex topological changes, the CSF model is superior to the conventional method in robustness and versatility. However, it is not without drawbacks. The CSF model has been found to generate vortex-like flows, referred to as spurious currents in the literature, in the neighborhood of the interface [5–12]. When the surface tension forces are dominant, these vortex-like currents may destroy the interface and cause disruptive instabilities at the interface. This often results in failure of convergence on grid refinement.

In a continuum method, discontinuities such as surface tension are usually smoothed out over a finite thickness involving several layers of computational cells. This smoothing of a discontinuity can be detrimental and can result in numerical errors that worsen with increasing width of the smoothing region. On a fixed orthogonal grid, the mass contained in a given cell is accelerated by the body force. In the transition region, the body force and the mass often do not vary at the same rate. While the mass approaches a small value near the free surface, the body force may still maintain a relatively large value. This will lead to an increase in flow acceleration and consequently the formation of spurious currents. Another cause for the spurious currents is the numerical imbalance between the surface tension force and the associated pressure gradient, which is especially significant in the Eulerian-based formulations on a fixed grid.

Great efforts have been made in recent studies [6–12] to reduce the spurious currents and improve on the modeling of the surface tension. In general, the accuracy of the curvature estimation and the implementation of the surface tension force are two key areas of focus. Popinet and Zaleski [6] improved the pressure gradient calculation by a pressure gradient correction procedure in their front-tracking method. Torres and Brackbill [7] employed a curl projection method for incompressible flows to reduce the spurious currents with an unconnected front-tracking method. Based on the VOF method, Meier et al. [8] devised a new technique, which used empirical formulas obtained from databases that had been generated and stored in a data bank to determine interface curvatures. It was found that the choice of density at the interfacial cells significantly affected the spurious currents. This is because the denser fluid and the lighter fluid experience different accelerations at the interfacial cells. Shirani et al. [9] attempted to remedy this issue by multiplying the body force (Eq. (2)) by a factor H which denotes the area of a cell face in contact with the heavier liquid. Brackbill et al. [4] also suggested adding a density scaling factor to the body force. Renardy and Renardy [10] developed a parabolic reconstruction of surface tension (PROST) method by using a quadratic representation of the surface with a least-square fit to the VOF functions along with a body force algorithm similar to the CSF model. Their method was based on the premise that the discrete pressure gradient be exactly balanced by the body force term at the discrete level. The similar idea was adopted by Shin et al. [11] who presented a new hybrid technique for surface tension calculation in the context of the front-tracking method, which combined the Lagrangian and Eulerian representation of surface tension force in a manner analogous to the VOF-CSF form. In a more recent study [12] by Francois et al., a balanced-force algorithm for the Navier–Stokes equations was described and it was used in conjunction with both the continuous and sharp surface tension models within a volume tracking framework. The key point of their algorithm is that both the surface tension force term and the pressure gradient were estimated at the cell faces. It was demonstrated that an exact balance of surface tension and pressure gradient forces could be achieved when the curvature was known accurately.

While improvements to the surface tension model have been made in the above studies, surface tension is still being treated as a body force or as a source term in the momentum equation. The inherent problem

resulted from the smoothing of the surface discontinuity in a continuum formulation previously mentioned remains unresolved. Jamet et al. [13] developed a very promising approach which can completely eliminate the spurious currents. They concluded that the essential requirement for the elimination of parasitic currents was energy conservation. But this approach was only applicable within the framework of the second-gradient method.

Some methods [14–16] have appeared recently which treated the jump discontinuities at the interface in a sharp way. The ghost fluid method (GFM) was developed for two-phase compressible inviscid flows [14], which allowed a sharp change in density without any smearing. In this method, ghost cells were used to define each fluid at every point in the computational domain. Each grid point contained the flow variables for the real fluid that existed at that point and ghost variables for the other fluid that did not actually exist at that point. Each fluid was updated separately and the velocity and pressure were treated as continuous across the interface without any jump conditions considered. These ideas were later extended [15] to three-dimensional multiphase incompressible flows taking into consideration the physical effects of viscosity and surface tension. The method presented by Helenbrook et al. [16] maintained the discontinuous properties at the interface without any artificial smoothing. A special treatment of the jump conditions with a higher order extrapolation procedure was adopted when solving the flow equations. However, it was not applicable to viscous flows with the jump conditions that involved spatial derivatives of the flow variables at the discontinuity. It should be noted that the LS method was used in the above studies to track the interface where the precise sub-cell interface location was obtained. As discussed later in this paper, the LS method suffers from loss of accuracy in mass conservation.

The objective of the present study is to improve on the numerical modeling of the surface tension force for capillarity-dominant free surface flows. A new surface tension implementation algorithm, referred to as the pressure boundary method (PBM), is introduced. The surface tension force is incorporated into the Navier–Stokes equation via a capillary pressure gradient term in the first step of a two-step projection method while the free surface is tracked by a coupled level set and volume-of-fluid (CLSVOF) method.

It has been shown in a stationary droplet benchmark test that the spurious currents are greatly reduced by the present method with sharp pressure boundary conditions preserved. In another standard test, an initially elliptical drop oscillating to an equilibrium state is modeled. To serve as a test on the dynamic performance of the present algorithm, a falling droplet impinging onto a substrate is simulated. The PBM algorithm has also been applied to study the relaxation dynamics of an elongated ligament where the droplet pinch-off mechanism is examined. The numerical results are in good agreement with results reported in the literature. A brief overview of the governing equations and the CLSVOF free surface tracking scheme is given in Sections 2 and 3, respectively, followed by an in-depth discussion of the surface tension implementation algorithm in Section 4. Finally, numerical results and discussion are presented in Section 5.

2. Governing equations

For incompressible flows with constant properties, the continuity and the Navier–Stokes equations are given by:

$$\nabla \cdot \vec{V} = 0 \tag{3}$$

$$\frac{\partial \vec{V}}{\partial t} + \nabla \cdot (\vec{V}\vec{V}) = -\frac{1}{\rho}\nabla p + \frac{1}{\rho}\nabla \cdot \tau + \vec{g} \tag{4}$$

where $\vec{V}$ is the velocity, ρ the density, p the pressure, τ the viscous stress tensor and $\vec{g}$ the gravitational acceleration. For Newtonian fluids, the stress tensor, τ, can be written as

$$\tau = 2\mu S \tag{5}$$

where S is the strain rate tensor given by:

$$S = \frac{1}{2}[(\nabla \vec{V}) + (\nabla \vec{V})^{\mathrm{T}}] \tag{6}$$

Eq. (4) is then discretized as

$$\frac{\vec{V}^{n+1}-\vec{V}^{n}}{\delta t}=-\nabla\cdot(\vec{V}\vec{V})^{n}-\frac{1}{\rho^{n}}\nabla p^{n+1}+\frac{1}{\rho^{n}}\nabla\cdot\tau^{n}+\vec{g}^{n} \tag{7}$$

where the superscripts n and $n+1$ represent the value of the variable at consecutive time steps. The only implicit term in the above equation is the pressure. Gravity, advection, and viscosity are approximated with old values at time t^n. A two-step projection method is used where Eq. (7) is decomposed into two equations to be solved consecutively. Details of the projection method in conjunction with the surface tension implementation scheme are given in Section 4.

3. CLSVOF scheme

As mentioned earlier, the VOF and the LS methods are two Eulerian-based method, which have been widely used to implicitly track the interface. One of the advantages of these methods is that they can easily handle flow problems with large topological changes and interface deformations such as liquid ligament breakup, bubble merging and bursting, and droplet elongation and breakup. The VOF method has the desirable property of mass conservation. However, it lacks accuracy in the normal and curvature calculations due to discontinuous spatial derivatives of the VOF function near the interface. On the other hand, the normal and curvature can be calculated accurately from the smooth continuous distance functions in the LS method. One serious drawback of the LS method is the frequent violation of the mass conservation. To overcome such weaknesses of the LS method and the VOF method, the coupled level set and volume-of-fluid (CLSVOF) method has recently been explored [17–20].

In general, the interface is reconstructed via a piecewise linear interface construction (PLIC) scheme from the VOF function and the interface normal vector computed from the LS function. By taking advantage of both the VOF and LS methods, the CLSVOF method is able to compute the normal and curvature more accurately while satisfying mass conservation. It should be mentioned that the implementation of the PLIC scheme is not unique as various implementation algorithms have been reported. The same is true with the LS method where different re-distance implementation schemes have been used. In the present study, the PLIC scheme presented by Rudman [5] is used and the LS re-distance algorithm proposed by Son [19] is followed. A brief overview is given here. Details can be obtained from the references.

The LS function, ϕ, is defined as a signed distance function whose magnitude equals the shortest distance from the interface with its sign given by:

$$\phi(\vec{x},t)\begin{cases}>0, & \text{outside of the interface}\\ =0, & \text{at the interface}\\ <0, & \text{inside the interface}\end{cases} \tag{8}$$

The VOF function, F, is defined as the liquid volume fraction in a cell with its value between zero and one in a surface cell and at zero and one in air and liquid, respectively, i.e.

$$F(\vec{x},t)=\begin{cases}1, & \text{in the fluid}\\ 0<F<1, & \text{at free surface}\\ 0, & \text{external to fluid}\end{cases} \tag{9}$$

The LS function and the VOF function are advanced, respectively, by the following equations:

$$\frac{\partial\phi}{\partial t}=-(\vec{V}\cdot\nabla)\phi \tag{10}$$

$$\frac{\partial F}{\partial t}=-(\vec{V}\cdot\nabla)F \tag{11}$$

Since the VOF function is not smoothly distributed at the free surface, an interface reconstruction procedure is required to evaluate the VOF flux across a cell containing a free surface. In this study, the interface is reconstructed by following a PLIC scheme [5] and the interface normal is calculated from the LS function given by:

$$\vec{n} = \frac{\nabla\phi}{|\nabla\phi|} = \nabla\phi \tag{12}$$

The LS function will fail to be a distance function after being advanced by Eq. (10) and a re-initialization process [3] is needed for its return to a distance function. This can be achieved by obtaining a steady-state solution of the following re-initialization equation:

$$\frac{\partial\phi}{\partial t} = \frac{\phi_0}{\sqrt{\phi_0^2 + h^2}}(1 - |\nabla\phi|) \tag{13}$$

where ϕ_0 is the LS function at the previous time step, t the artificial time, and h the grid spacing. In order to achieve mass conservation, the LS functions have to be re-distanced [19,20] prior to being used. This is done by calculating the distance geometrically from the cell center to the reconstructed interface. Finally, the surface curvature can be computed directly from the LS function and is given by:

$$\kappa = \nabla \cdot \nabla\phi \tag{14}$$

4. Surface tension implementation

A new surface tension implementation algorithm, referred to as the pressure boundary method (PBM), is introduced in this study. The surface tension force is incorporated into the Navier–Stokes equation via a pressure gradient term. Basically, the pressure term is separated into two components: one for the surface tension and the other for achieving mass conservation. This enables the surface tension induced sharp pressure conditions at the free surface to be preserved.

The two-step projection method [22] is used where the momentum equation given by Eq. (7) is decomposed into the following two equations:

$$\frac{\vec{\tilde{V}} - \vec{V}^n}{\delta t} = -\nabla \cdot (\vec{V}\vec{V})^n + \frac{1}{\rho^n}\nabla \cdot \tau^n + \vec{g}^n - \frac{1}{\rho^n}\nabla p_1 \tag{15}$$

and

$$\frac{\vec{V}^{n+1} - \vec{\tilde{V}}}{\delta t} = -\frac{1}{\rho^n}\nabla p_2 \tag{16}$$

where $\vec{\tilde{V}}$ represents an intermediate velocity and

$$p^{n+1} = p_1 + p_2 \tag{17}$$

Prior to the execution of the two-step projection procedure, p_1 is first computed from the following equation:

$$\nabla \cdot \left[\frac{1}{\rho^n}\nabla p_1\right] = 0 \tag{18}$$

along with the pressure boundary condition at the free surface given by:

$$p_v - p + \sigma\kappa = -2\mu n\frac{\partial u}{\partial n} \tag{19}$$

where κ is the local free surface curvature, σ the surface tension coefficient, p_v the vapor (gas) pressure, n the free surface normal, and u the velocity. At the free surface, viscous effects are negligible and Eq. (19) is reduced to the Laplace's formula:

$$p - p_v = \sigma\kappa \tag{20}$$

The Dirichlet boundary condition at the free surface then becomes:

$$p_S = p_v + \sigma\kappa_s \tag{21}$$

where p_S is the liquid side interface pressure, which is used as the boundary value for p_1 in Eq. (18). κ_s is the curvature at the free surface, which is interpolated from the cell-centered values calculated by Eq. (14).

In the first step of the projection method, an intermediate velocity field $\vec{\tilde{V}}$ is computed from Eq. (15). The second step involves taking the divergence of Eq. (16) while imposing the incompressibility condition on the velocity field $\vec{V}^{n+1}$:

$$\nabla \cdot \vec{V}^{n+1} = 0 \tag{22}$$

This results in the following Poisson equation for p_2:

$$\nabla \cdot \left[\frac{1}{\rho^n}\nabla p_2\right] = \frac{\nabla \cdot \vec{\tilde{V}}}{\delta t} \tag{23}$$

The velocity field $\vec{V}^{n+1}$ is then updated via Eq. (16) and the pressure p^{n+1} from Eq. (17). A flow chart for the overall computational cycle is given in Fig. 1.

The solution of Eq. (18) with the sharp pressure boundary condition is a key element of the PBM algorithm, which involves a special treatment of the discretization at the interface. The finite difference scheme employed by Gibou et al. [21] is adopted in the present study. Due to the jump condition across the interface,

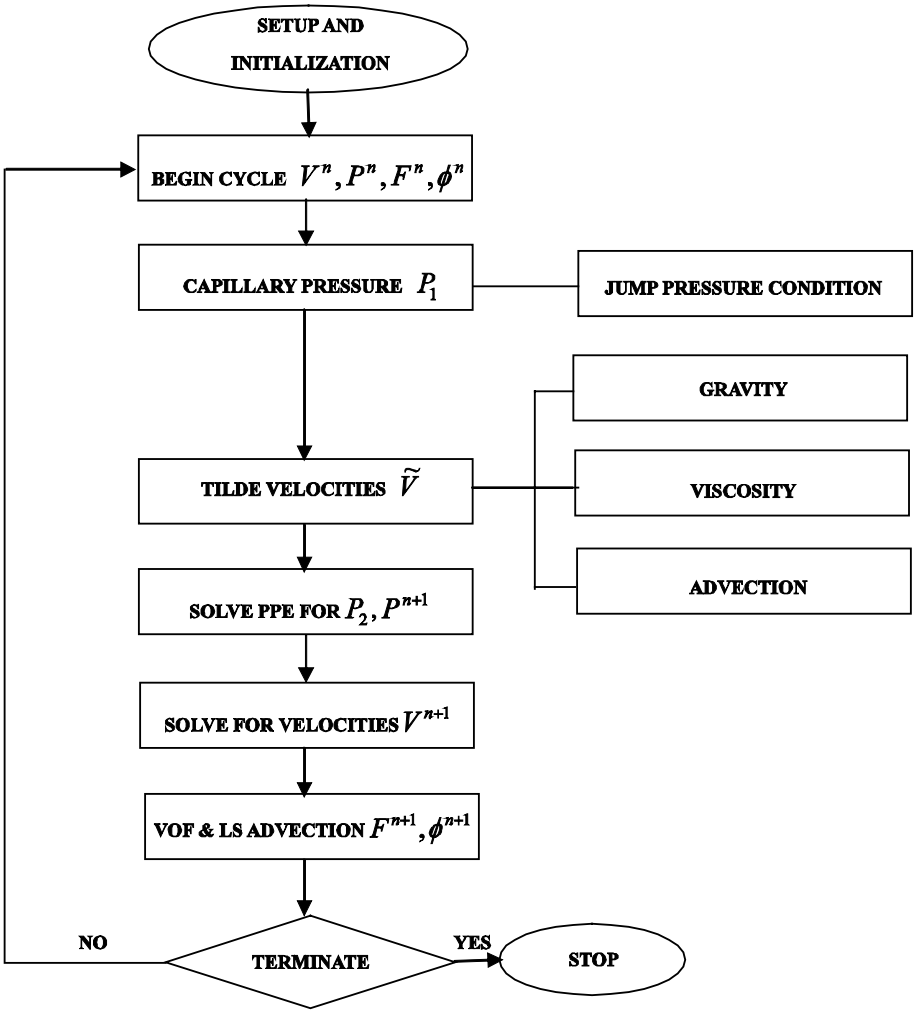

Fig. 1. Flow diagram for one computational cycle.

pressure p_1 is only defined in the liquid side. With reference to Fig. 2, the pressure gradients at the faces of cell (i,j) are given by:

$$\left(\frac{\partial p_1}{\partial x}\right)_{i+1/2,j} = \frac{(p_1)_{Sr} - (p_1)_{i,j}}{\theta_r \Delta x} \tag{24a}$$

$$\left(\frac{\partial p_1}{\partial x}\right)_{i-1/2,j} = \frac{(p_1)_{i,j} - (p_1)_{i-1,j}}{\Delta x} \tag{24b}$$

$$\left(\frac{\partial p_1}{\partial y}\right)_{i,j+1/2} = \frac{(p_1)_{St} - (p_1)_{i,j}}{\theta_t \Delta y} \tag{24c}$$

$$\left(\frac{\partial p_1}{\partial y}\right)_{i,j-1/2} = \frac{(p_1)_{i,j} - (p_1)_{i,j-1}}{\Delta y} \tag{24d}$$

where $(p_1)_{Sr}$ and $(p_1)_{St}$ are liquid pressures at the free surface given by Eq. (21). θ is the fraction of the distance from the interface to the center of cell (i,j) given by:

$$\begin{aligned} \theta_r &= \frac{|\phi_{i,j}|}{|\phi_{i,j}| + |\phi_{i+1,j}|} \\ \theta_t &= \frac{|\phi_{i,j}|}{|\phi_{i,j}| + |\phi_{i,j+1}|} \end{aligned} \tag{25}$$

with the LS function, ϕ, serving as the distance function. Since p_1 is undefined at the exterior points, $(p_1)_{Sr}$ and $(p_1)_{St}$ are used in Eqs. (24a) and (24c) for the pressure gradients instead of $(p_1)_{i+1,j}$ and $(p_1)_{i,j+1}$, respectively. This treatment allows the sharp pressure jump to be well preserved without any smoothing. For everywhere else inside of the free surface, standard finite-difference forms, given by Eqs. (24b) and (24d), are used. Note that the same discretization procedure should be followed when approximating pressure gradients in Eq. (15), as this is essential to ensure the balance between the surface force and the pressure gradients.

Eq. (18) takes the following form after discretization:

$$\nabla \cdot \left[\frac{1}{\rho}\nabla p_1\right]_{i,j} = \frac{\left(\frac{1}{\rho}\frac{\partial p_1}{\partial x}\right)_{i+1/2,j} - \left(\frac{1}{\rho}\frac{\partial p_1}{\partial x}\right)_{i-1/2,j}}{\Delta x} + \frac{\left(\frac{1}{\rho}\frac{\partial p_1}{\partial y}\right)_{i,j+1/2} - \left(\frac{1}{\rho}\frac{\partial p_1}{\partial y}\right)_{i,j-1/2}}{\Delta y} = 0 \tag{26}$$

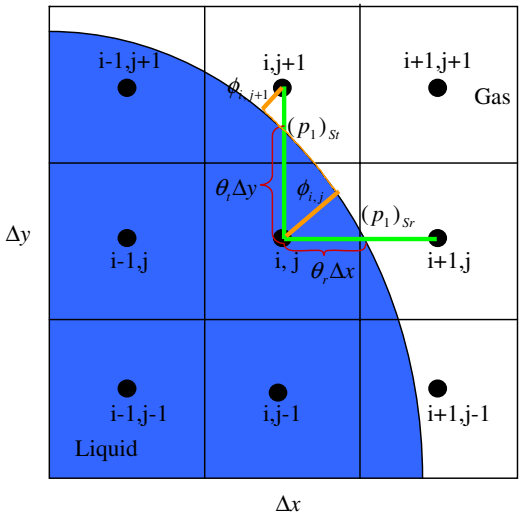

Fig. 2. Discretization of pressure gradient at the interface, and determination of the distance fraction θ.

Substitutions of Eqs. (24a)–(24d) into Eq. (26) result in a symmetric form for p_1, which can be solved readily by using an incomplete Cholesky conjugate gradient (ICCG) method [22]. Note that although density is constant for incompressible fluids, it is retained inside the divergence operator. It has been found that better grid convergence with reduced numerical errors can be achieved by treating the density as a variable at the free surface. The density is weighted by the VOF function in the present study.

As for p_2, Eq. (23) can be discretized by the standard discretization method without utilizing the special treatment adopted for p_1. As shown in Fig. 2, although nodes $(i+1,j)$ and $(i,j+1)$ are in the gas side, the mass in these computational cells is non-zero. At the discrete level, velocity is continuous across the interface, which means velocity is still defined and valid in these cells. As previously mentioned, p_2 is used to account for mass conservation and is induced by flow motion. This implies that p_2 must also be continuous across the interface and be defined in these cells. For the void cells, such as cell $(i+1,j+1)$, p_2 is constant (taken as zero here) and serves as the boundary condition for Eq. (23). Thus, the discretization of Eq. (23) is relatively straightforward, which also results in a symmetric form and the same ICCG technique [22] can be applied as in the solution for p_1.

5. Numerical tests and simulation results

To validate the PBM algorithm, four numerical experiments have been conducted. First, a stationary droplet is employed to test the static performance, followed by an oscillating droplet test and the impingement of a falling droplet onto a substrate. Finally, the relaxation process of an elongated liquid droplet is studied which serves as an example for capillarity-dominant flows.

5.1. A stationary droplet in air

A stationary spherical droplet without gravity is often used in the literature to test surface tension algorithms for spurious currents [8]. Theoretically, in the absence of external forces and initial velocities, the velocity field should remain zero throughout. However, spurious currents have been found in many surface tension simulation methods [1,5–13].

In the present study, calculations are performed on an axisymmetric computational domain of 1.0 mm × 2.0 mm. Water at room temperature and standard atmospheric conditions are used. For comparison purposes, the CSF method is also included in the computations. It is used in conjunction with both the CLSVOF and the VOF algorithms. The maximum and mean magnitudes of the velocity at 0.5 ms for the different methods are given in Table 1.

As shown in Table 1, with the CSF model, the CLSVOF method produces less spurious current than the VOF method and is thus a better method. This is perhaps not surprising since the estimation of the curvature in the CLSVOF method is more accurate than that in the VOF method. With the CLSVOF method, it is clear that the PBM method gives better results than the CSF method with significantly reduced spurious currents.

Table 1
Maximum and mean velocity magnitude after 0.5 ms, time step, $\Delta t = 1.0e-4, 1.0e-5, 1.0e-6$ for three grids, respectively

Method	$\Delta x \times \Delta y$ (mm × mm)	Maximum magnitude (mm/ms)	Mean magnitude (mm/ms)
VOF-CSF	0.04 × 0.04	0.3641080	0.00899505
	0.02 × 0.02	0.4120642	0.00558990
	0.01 × 0.01	0.5095969	0.00564543
CLSVOF-CSF	0.04 × 0.04	0.2005396	0.00398587
	0.02 × 0.02	0.2829645	0.00207592
	0.01 × 0.01	0.2539782	0.00108487
CLSVOF-PBM	0.04 × 0.04	0.0067001	6.3110e − 005
	0.02 × 0.02	0.0037879	1.1087e − 005
	0.01 × 0.01	0.0000000	0.0000e − 005

Fig. 3 shows the maximum and mean velocity magnitudes versus time plots for the three different methods with various grid sizes. It can be seen that for both CSF models, i.e. VOF-CSF and CLSVOF-CSF, the magnitude of the velocity increases with time initially and starts fluctuating afterwards. On the other hand, the magnitudes of the spurious currents in the CLSVOF-PBM method are under control throughout.

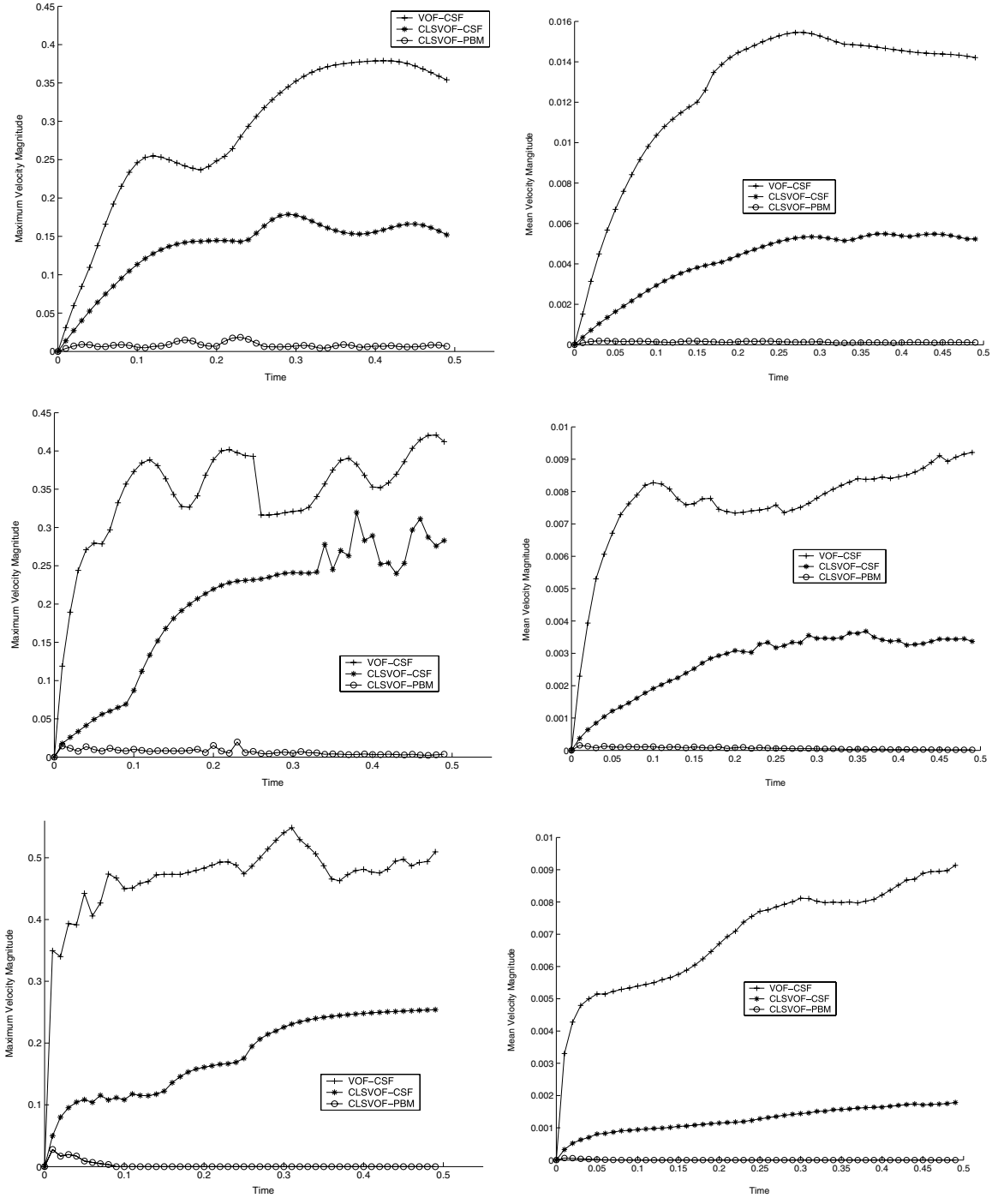

(Maximum velocity) (Mean velocity)

Fig. 3. Maximum and mean velocity magnitude versus time. Grid spacing at top: 0.04×0.04; middle: 0.02×0.02; bottom: 0.01×0.01.

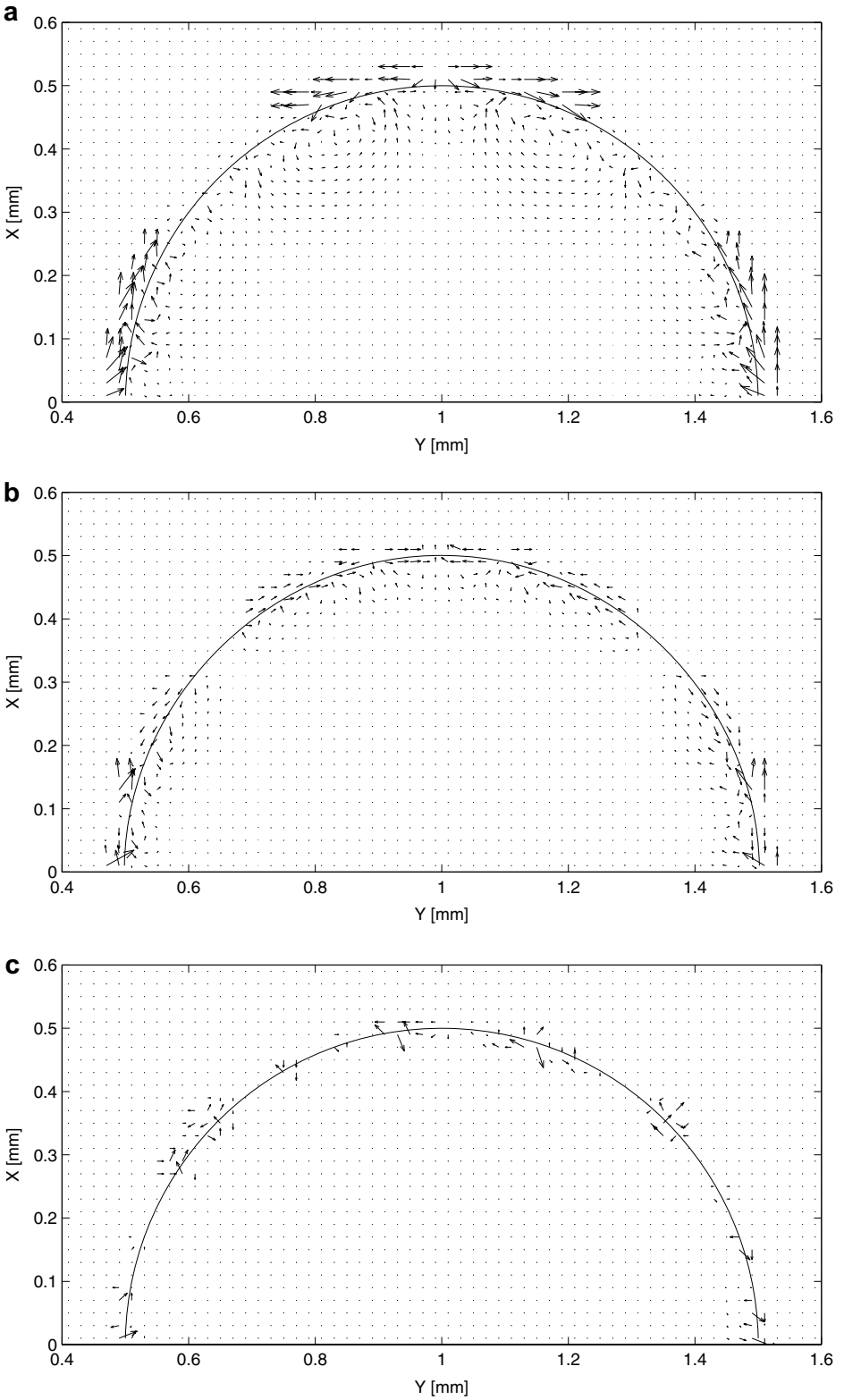

Fig. 4. Velocity profiles for a stationary droplet at 0.5 ms. Grid: 0.02×0.02. (a) VOF-CSF; (b) CLSVOF-CSF; (c) CLSVOF-PBM.

Fig. 4 shows the velocity profiles for the three different cases. Strong spurious currents can be seen in the vicinity of the free surface for both the VOF-CSF and CLSVOF-CSF methods but are drastically suppressed for the CLSVOF-PBM method. The pressure distributions are shown in Fig. 5. For the CSF method, it can be seen that the pressure smears over 3–4 computational cells in the transition region across the interface where it changes gradually from the ambient pressure (taken as zero) to the jump pressure ΔP ($=\sigma\kappa$). As for the

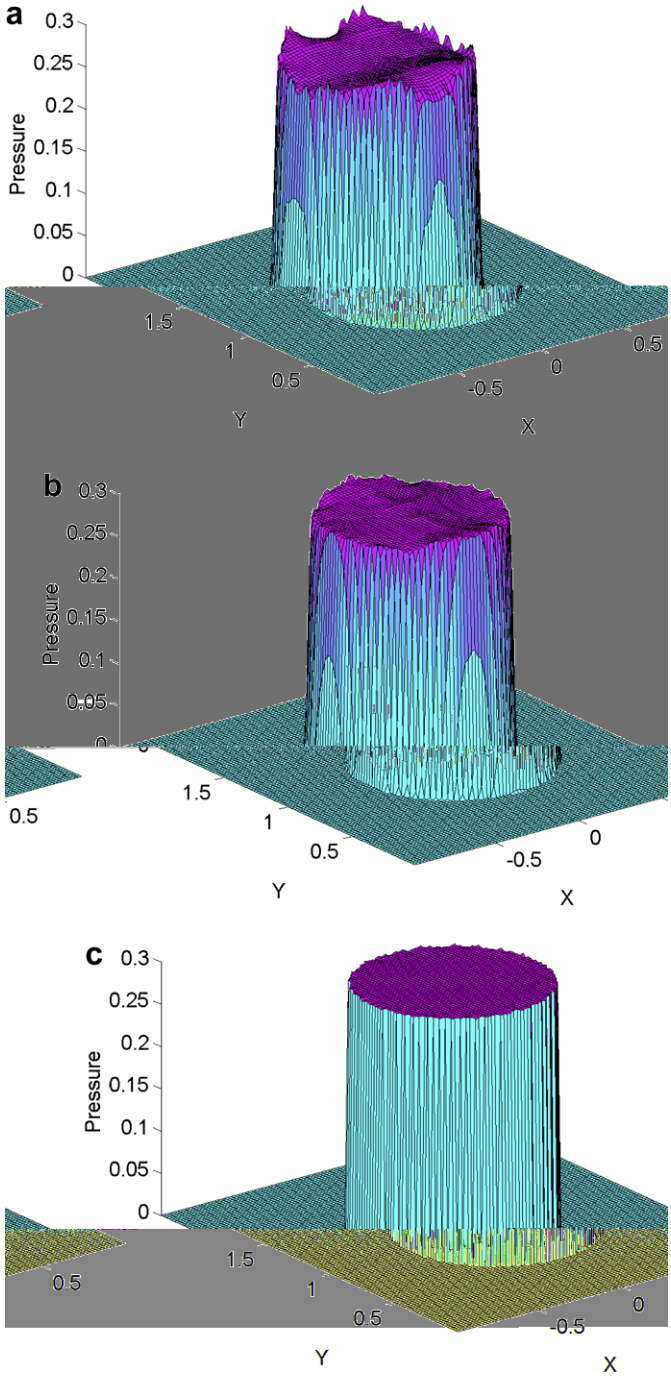

Fig. 5. Pressure distribution for a static droplet at time 0.5 ms: (a) VOF-CSF; (b) CLSVOF-CSF; (c) CLSVOF-PBM.

CLSVOF-PBM method, the pressure changes sharply across the interface and remains rather uniformly distributed inside the drop.

In the CSF model, non-zero pressure gradients are generated in the transition region across the interface due to the smearing nature of the pressure. These non-zero pressure gradients are not well balanced by the body force in the transition region. Consequently, unphysical currents will inevitably be present in the region. This modeling of the surface tension effect is not consistent with the associated sharp pressure jump condition at the interface. In the PBM method, the surface tension effect is treated as a sharp pressure boundary condition located exactly at the free surface rather than at the adjacent grid locations (center or face). The surface-tension-induced pressure field is solved directly without any artificial smoothing. This ensures the pressure jump to be well balanced by the surface tension force at the interface of the static drop. As a result, a relatively uniform pressure field is obtained with very small pressure gradients throughout the droplet. The sharp pressure jump condition at the free surface is preserved and the undesirable spurious currents are significantly reduced.

5.2. Oscillating drops

As another standard and demanding test, an initially non-spherical viscous drop with subsequent oscillating decay to equilibrium static shape is often used [7,11,12] for surface tension modeling methods. In the present study, the same test case is considered as in [7,12] except that the surrounding phase is neglected. An elliptical liquid drop, specified by the equation $x^2/9 + y^2/4 = 1$, is initially placed at the center of a 20×20 computational domain in the absence of gravity. The liquid properties are chosen as density $\rho = 1.0$, viscosity $\mu = 0.01$ and surface tension $\sigma = 1.0$. For comparison purposes, the CSF method in conjunction with the CLSVOF scheme is also included in the computations.

Due to the surface tension force, the elliptical drop oscillates and finally reaches an equilibrium static state (spherical shape) by the damping effect of viscosity. The kinetic energy, $\frac{1}{2}\int \rho \vec{V} \cdot \vec{V}\, dv$, versus time plots are shown in Fig. 6. It is clear that the drop fails to reach a static state due to the spurious currents effect with the CSF method. As for the PBM method, the kinetic energy decays gradually and a final static state is reached. The oscillation frequency of the drop with the PBM method is similar to that reported in [7,12]. The maximum amplitude of the oscillation is slightly lower than those reported in [7,12], and the difference is due to the neglect of the dynamics of the surrounding phase in the present study. Velocity profiles for the two methods at various time instants are shown in Fig. 7. At the early oscillating stage, the velocity fields in both the CSF and PBM methods are very close, as the parasitic currents are masked due to the dynamic

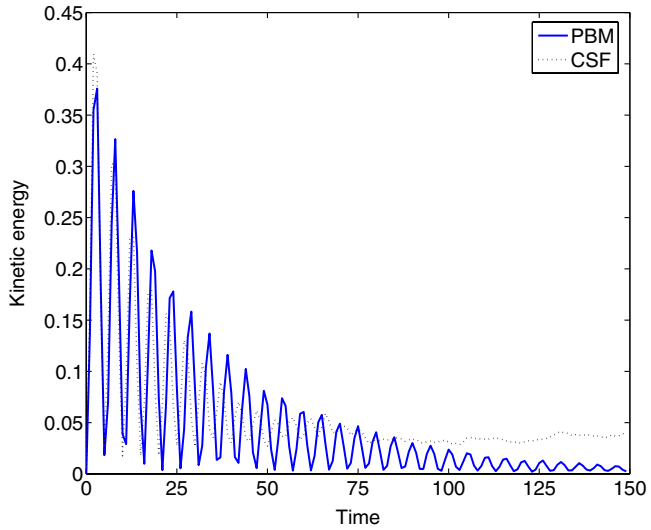

Fig. 6. Kinetic energy versus time plot for a 2D oscillating drop. Grid: 0.3125×0.3125.

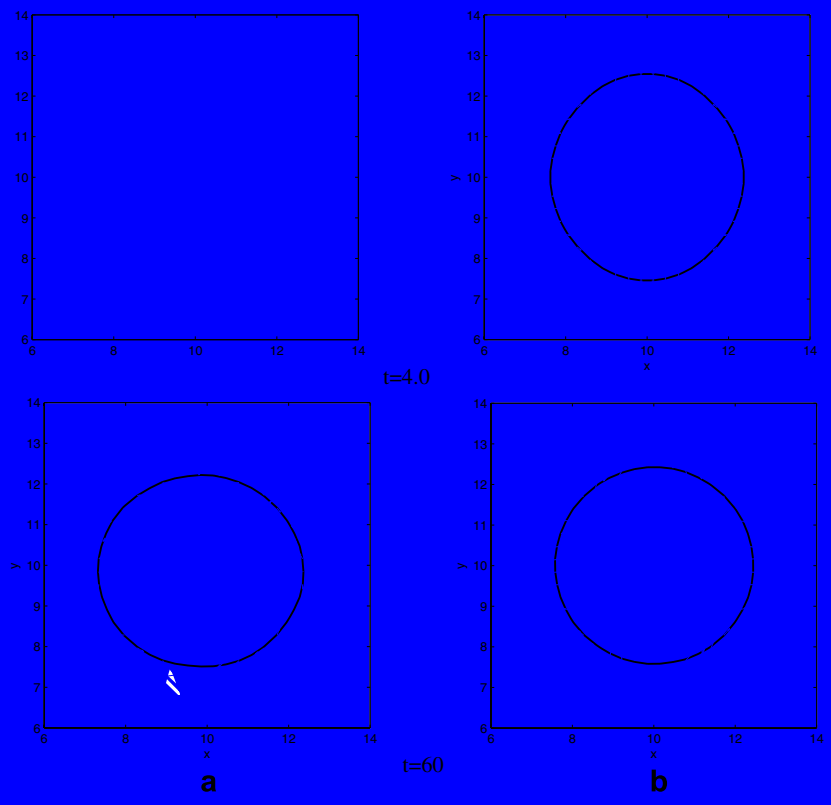

Fig. 7. Velocity profiles for a 2D oscillating drop: (a) CSF; (b) PBM.

situation.
regular flo

This is
methods s
by Franco
breakup a
Torres and
The results
reported by

5.3. A fallin

A falling
ent algorith
dynamic situ
that an accep
ditions. Wate
Droplet surfa
prior to the in
shown at the

For droplet
with negligible
and PBM met

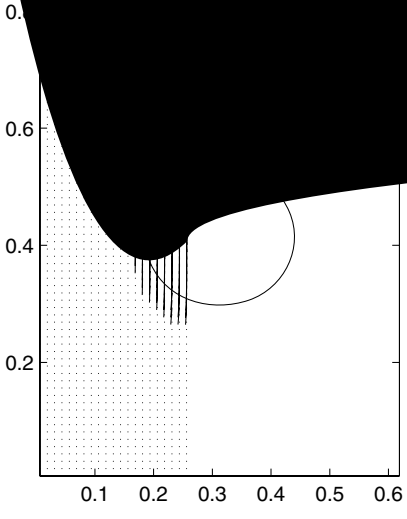

be due to the fact that the flows are highly dynamic within the droplet and spurious currents are relatively insignificant. Nevertheless, the results demonstrate the capability of the PBM scheme in such a dynamic simulation.

5.4. Relaxation of a moderately elongated liquid ligament

Finally, the relaxation process of a moderately elongated liquid ligament is simulated. This is a good example for capillarity-driven free surface flows where the fluid motion is driven by surface tension forces associated with curvature variations along the ligament free surface. As the flow is surface tension driven and involves complex topological changes (e.g., breakup), accurate modeling of the surface tension force is critical. Although fix-grid methods such as the VOF have the capability of handling topologically challenging interface problems, they often suffer a lack of accuracy due to imprecise interface information in the simulation of such flows [1]. This may cause problems in grid convergence. The initial configuration of the elongated ligament is shown in Fig. 9. It is 13.6 mm in length with a radius of 0.3 mm at the cylindrical portion. The bulbous elliptical end shape is based on the experimental findings of Stone et al. [23]. It is observed that breakup occurs due to deterministic flows established by capillary forces associated with curvature variations along the interface, rather than by the classical capillary-wave instability. The observed motion consists of a relatively rapid bulging of the end of the ligament followed by break-off of the bulbous end from the central region of the ligament. This end pinching phenomenon has also been observed in an experimental investigation of the binary droplet collision dynamics by Qian and Law [25].

In order to conserve computational resources, only half of the ligament is considered and the computations are conducted on an axisymmetric domain with dimensions of 7.0 mm × 1.0 mm. Water with same fluid properties as in the previous tests is used with the exception that the surface tension is 1000 times higher. This results in a very rigorous situation for surface tension modeling with a Laplace number $La = \sigma\rho R/\mu^2$ of the order of 10^7. The spurious currents effect is magnified and may grow and cause catastrophic interface instabilities [1]. Again, VOF-CSF, CLSVOF-CSF and CLSVOF-PBM are all included for comparison. The relaxation sequence leading to the break-up is shown in Fig. 10. The numerical results are in excellent agreement with the ''end-pinching'' mechanism outlined in details by Stone et al. [23,24] and Qian and Law [25]. A brief description of the mechanism is given below.

The additional curvature at the rounded ends of the ligament, as compared to the central portion, generates a higher pressure because of surface tension. The pressure gradient pushes the fluid away from the ends towards the midsection, resulting in the formation of a bulbous region at the tips. The presence of the bulb leads to a negative curvature and consequently a minimum pressure somewhere between the bulbous end and the midsection, setting up a local flow towards this minimum pressure point from the midsection side. The local flow creates a neck as a result of local mass reduction accompanying the flow. The formation of this neck leads to an increase in pressure due to the increase in curvature by the reduction of local ligament radius. This local peak in pressure sets off fluid flows in both directions away from the neck which results in a further reduction in the radius of the neck. This generates an unstable situation resulting in further development of the neck and an eventual end-pinch-off of the bulbous region.

Calculations have been made with four different meshes for grid convergence studies. As shown in Fig. 10, grid convergence fails in the VOF-CSF method, while it appears to have been achieved in the CLSVOF-CSF and CLSVOF-PBM methods. Fig. 11 shows the velocity fields at two time instants. In the CSF method, the

Fig. 9. Schematic representation of an elongated liquid ligament.

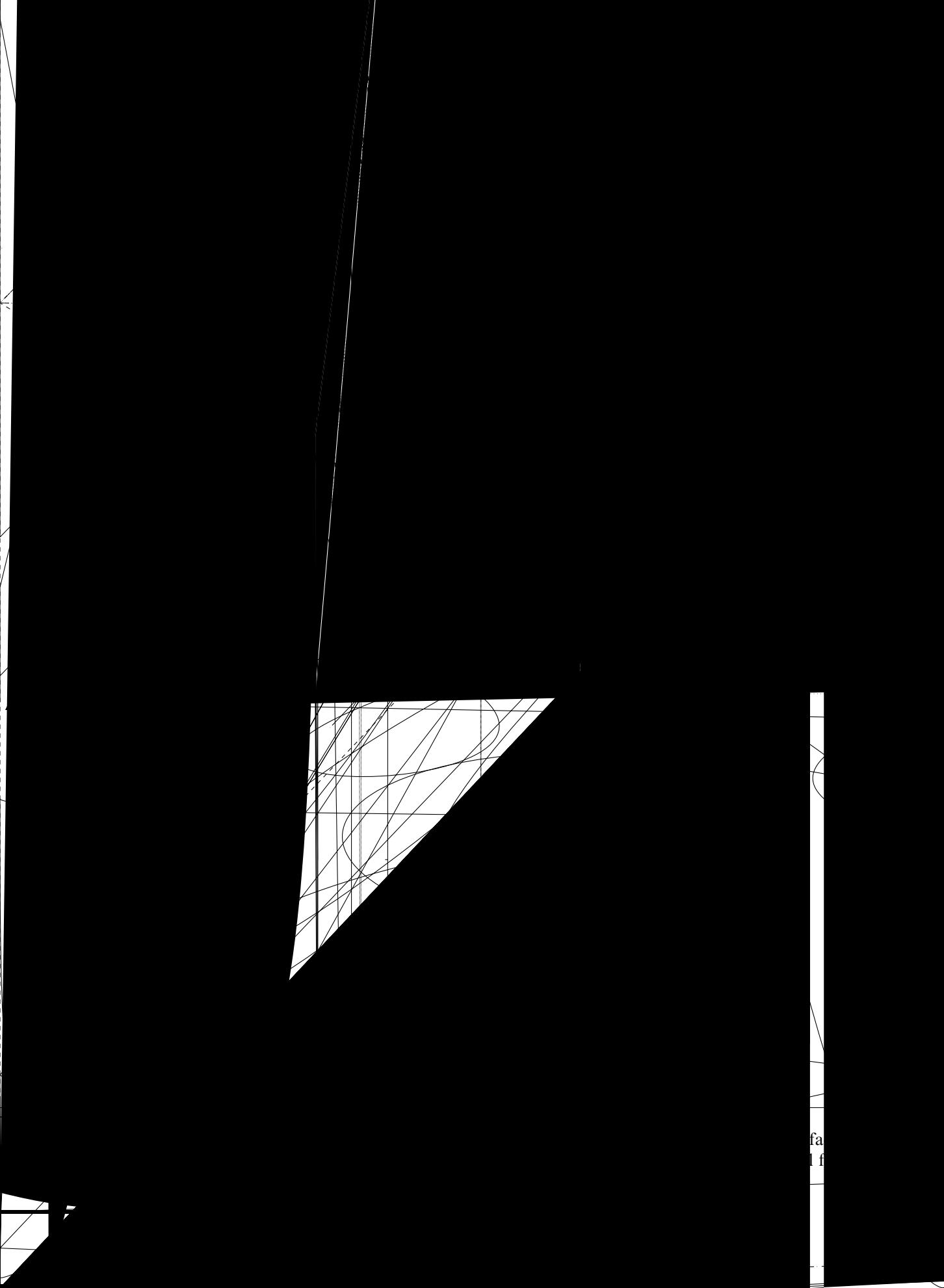

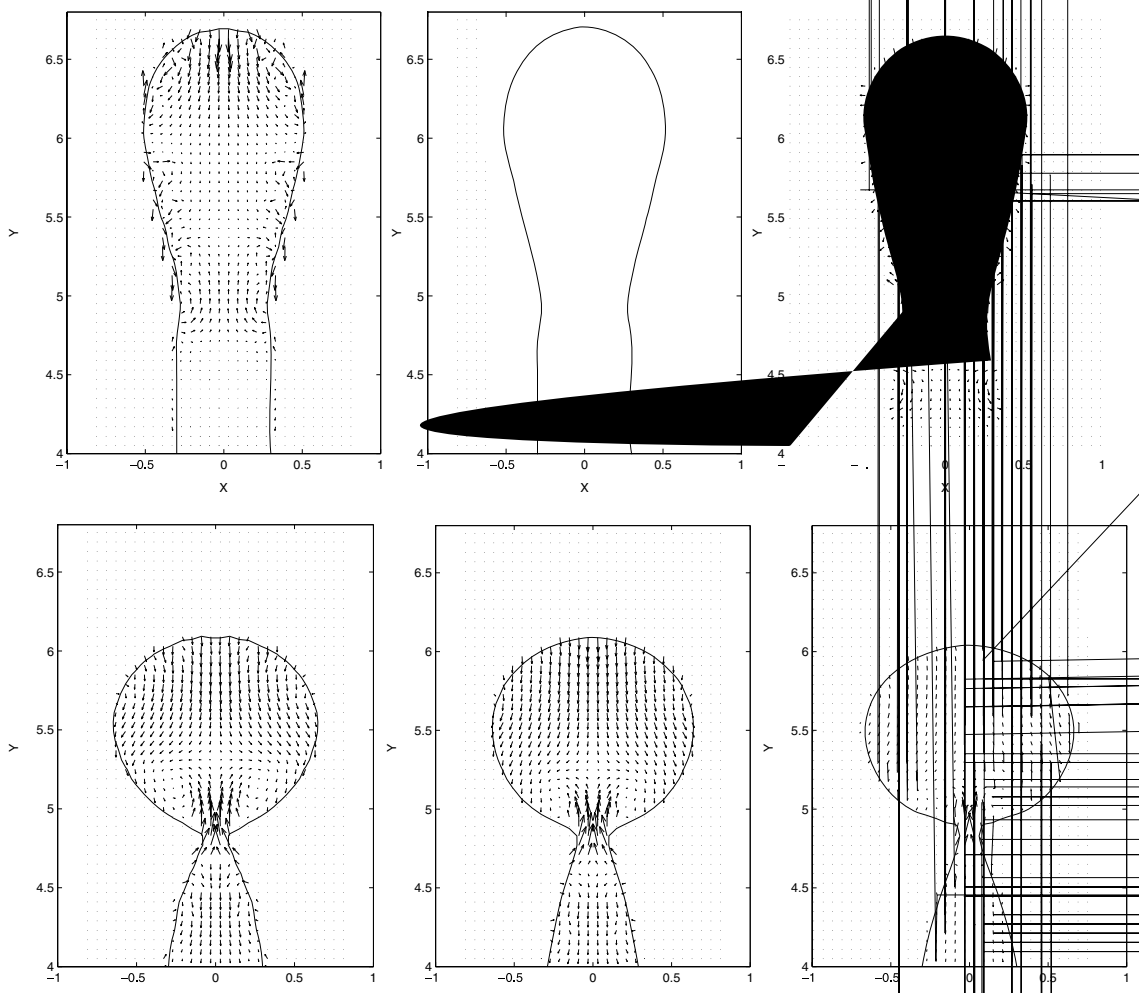

Fig. 11. Velocity profiles of an elongated ligament for different methods. Top row: earlier stage of the relaxation process; bottom row: immediately prior to the pinch-off occurrence.

In Table 2, the relative differences in the position of the interface (ligament volume is chosen here) between different grid sizes are shown. The relative differences of the interface position between successive grid sizes are used since the exact solution for this problem is not known. In the VOF-CSF method, the relative differences increase with mesh refinement, which indicates failure of the grid convergence. The relative differences diminish in both the CLSVOF-CSF and CLSVOF-PBM methods, with the PBM reducing at a faster pace.

Table 2
Relative differences of ligament volume between consecutively reduced grid sizes at one time instant

$\Delta x \times \Delta x$ (mm × mm)	VOF-CSF	CLSVOF-CSF	CLSVOF-PBM
0.0806×0.0806	N/A	N/A	N/A
0.0803×0.0803	0.1175	0.0841	0.1069
0.015×0.015	0.2048	0.0826	0.0716
0.0075×0.0075	0.2552	0.0741	0.0355

6. Conclusion

Numerical modeling of capillarity-driven free surface flows has been examined. The main focus is on the reduction of the undesirable spurious currents near the free surface. A new surface tension implementation algorithm, referred to as PBM, utilizing a capillary pressure gradient term in the Navier–Stokes equations, is introduced. A couple level set and volume-of-fluid method (CLSVOF) is used to track the free surface. It offers improved accuracy on the surface curvature and normal calculations while maintaining mass conservation. It has been shown in a stationary droplet benchmark test that the spurious currents have been greatly reduced by the present method with sharp pressure boundary conditions preserved. The PBM algorithm has also been applied to study the relaxation dynamics of an elongated ligament where the droplet pinch-off mechanism is examined. The numerical results are in good agreement with those reported in the literature.

References

[1] R. Scardovelli, S. Zaleski, Direct numerical simulation of free-surface and interfacial flow, Annu. Rev. Mech. 31 (1999) 567–603.
[2] C.W. Hirt, B.D. Nichols, Volume of fluid (VOF) method for the dynamics of free boundaries, J. Comput. Phys. 39 (1981) 201–225.
[3] M. Sussman, P. Smereka, S. Osher, A level set approach for computing solutions to incompressible two-phase flow, J. Comput. Phys. 114 (1994) 146–154.
[4] J.U. Brackbill, D.B. Kothe, C. Zemach, A continuum method for modeling surface tension, J. Comput. Phys. 100 (1992) 335–354.
[5] M. Rudman, A volume-tracking method for incompressible multifluid flows with large density variations, Int. J. Numer. Meth. Fluids 28 (1998) 357–378.
[6] S. Popinet, S. Zaleski, A front-tracking algorithm for the accurate representation of surface tension, Int. J. Numer. Meth. Fluids 30 (1999) 775–793.
[7] D.J. Torres, J.U. Brackbill, The point-set method: front-tracking without connectivity, J. Comput. Phys. 165 (2000) 620–644.
[8] M. Meier, G. Yadigaroglu, B.L. Smith, A novel technique for including surface tension in PLIC-VOF methods, Eur. J. Mech. B/Fluids 21 (2002) 61–73.
[9] E. Shirani, N. Ashgriz, J. Mostaghimi, Interface pressure calculation based on conservation of momentum for front capturing methods, J. Comput. Phys. 203 (2005) 154–175.
[10] Y. Renardy, M. Renardy, PROST: a parabolic reconstruction of surface tension for the volume-of-fluid method, J. Comput. Phys. 183 (2002) 400–421.
[11] S. Shin, S.I. Abdel-Khalik, V. Daru, D. Juric, Accurate representation of surface tension using the level contour reconstruction method, J. Comput. Phys. 203 (2005) 493–516.
[12] M.M. Francois, S.J. Cummins, E.D. Dendy, D.B. Kothe, J.M. Sicilian, M.W. Williams, A balanced-force algorithm for continuous and sharp interfacial surface tension models within a volume tracking framework, J. Comput. Phys. 213 (2006) 141–173.
[13] D. Jamet, D. Torres, J.U. Brackbill, On the theory and computation of surface tension: the elimination of parasitic currents through energy conservation in the second-gradient method, J. Comput. Phys. 182 (2002) 262–276.
[14] R. Fedkiw, T. Aslam, B. Merriman, S. Osher, A non-oscillatory Eulerian approach to interfaces in multimaterial flows (the ghost fluid method), J. Comput. Phys. 152 (1999) 457–492.
[15] M. Kang, R. Fedkiw, X.D. Liu, A boundary condition capturing method for multiphase incompressible flow, J. Sci. Compt. 15 (2000) 323–360.
[16] B.T. Helenbrook, L. Martinelli, C.K. Law, A numerical method for solving incompressible flow problems with a surface of discontinuity, J. Comput. Phys. 148 (1999) 366–396.
[17] A. Bourlioux, A coupled level-set volume-of-fluid algorithm for tracking material interfaces, in: Proceedings of the 6th International Symposium on Computational Fluid Dynamics, Lake Tahoe, CA, 1995, pp. 15–22.
[18] M. Sussman, E.G. Puckett, A coupled level set and volume-of-fluid method for computing 3D axisymmetric incompressible two-phase flows, J. Comput. Phys. 162 (2000) 301–337.
[19] G. Son, N. Hur, A coupled level set and volume-of-fluid method for the buoyancy-driven motion of fluid particles, Numer. Heat Transf. B 42 (2002) 523–542.
[20] G. Son, Efficient implementation of a coupled level-set and volume-of-fluid method for three-dimensional incompressible two-phase flows, Numer. Heat Transf. B 43 (2003) 549–565.
[21] F. Gibou, R. Fedkiw, L.T. Cheng, M. Kang, A second order accurate symmetric discretization of the Poisson equation on irregular domains, J. Comput. Phys. 176 (2002) 205–227.
[22] D.B. Kothe, R.C. Mjolsness, M.D. Torrey, RIPPLE: a computer program for incompressible flows with free surfaces, Technical Report, LA-12007-MS, Los Alamos National Laboratory, 1991.
[23] H.A. Stone, B.J. Bentley, L.G. Leal, An experimental study of transient effects in the breakup of viscous drops, J. Fluid Mech. 173 (1986) 131–158.
[24] H.A. Stone, L.G. Leal, Relaxation and breakup of an initially extended drop in an otherwise quiescent fluid, J. Fluid Mech. 198 (1989) 399–427.
[25] J. Qian, C.K. Law, Regimes of coalescence and separation in droplet collision, J. Fluid Mech. 331 (1997) 59–80.